Citation: Adam, H. A., T. Hayashida (2023), Estimation of crustal structure in northern Egypt using broadband seismic Ambient noise (5-50 s), Synopsis of IISEE-GRIPS Master's Thesis.

ESTIMATION OF CRUSTAL STRUCTURE IN NORTHERN EGYPT USING BROADBAND SEISMIC AMBIENT NOISE (5–50 s)

Hany Abuelnaga ADAM[1]
MEE22701

Supervisor: Takumi HAYASHIDA[2]

ABSTRACT

This study presents a comprehensive group velocity map for the crustal structure estimation in Northern Egypt using ambient noise tomography (ANT) focusing on periods from 5 to 50 s. The study area is located in Northern Egypt and encompasses regions bounded by the Red Sea to the east and the Mediterranean Sea. We collected seismic ambient noise data from 24 broadband seismic stations from July 2021 to June 2022, with an interstation spacing ranging from 50 to 1000 km. Green's Functions were derived from the cross-correlation of the recorded data, resulting in 276 station pairs for analysis. Accordingly, 100 to 250 reliable measurements were selected based on the signal-to-noise ratio and the standard deviation of seasonal dispersion curves. Utilizing the dense coverage of the ray paths enabled the generation of group velocity maps with 5 to 30 s periods, offering spatial resolutions between 50 and 400 km. The derived map revealed two distinct structural zones: a high-velocity zone in the eastern part and a low-seismic velocity zone in the western region. To further validate the results, one-dimensional shear wave velocity profiles were inverted from the observed group velocities. We found that the estimated Moho depths range from 40 km in the southwestern part to 35 km in the north and eastern parts. Our results show that ANT is a powerful and advantageous approach, particularly in nonactive seismic areas, effectively overcoming the challenges encountered in conventional receiver function analysis and seismic tomography.

Keywords: Seismic Ambient Noise, Rayleigh Wave, Group Velocity, Northern Egypt.

1. INTRODUCTION

Egypt is located in the northeastern corner of the African Plate, bordered by the eastern Mediterranean Sea to the north and the Red Sea to the east. The tectonic setting of the region is characterized by both divergent and convergent plate boundaries, interacting with the Arabian Plate and the Eurasian Plate, respectively. This convergence has resulted in the formation of significant geological features, such as the Hellenic Arc and the Cyprus Arc, which are subduction zones where the African Plate is undergoing downward displacement beneath the Eurasian Plate. The principal tectonic components influencing the geological landscape of Egypt are the African-Eurasian Plate margin, the Red Sea plate margin, and the Aqaba-Dead Sea transform fault (Collins et al., 2021). This research represents the initial effort to obtain the velocity structure of the crust and upper mantle in Egypt using Ambient Noise Tomography (ANT). Examining the crustal structure and a comprehensive understanding of geodynamic processes in this

[1] National Research Institute of Astronomy and Geophysics (NRIAG), Egypt.
[2] International Institute of Seismology and Earthquake Engineering, Building Research Institute (BRI).

area are important as they contribute to seismic hazard assessment and risk mitigation in Egypt. By shedding light on the subsurface characteristics and seismic properties, this study aims to provide valuable insights into the geological complexities of the region, potentially aiding in the development of more robust strategies for disaster preparedness and mitigation in the area.

2. DATA

We utilized one year of continuous record of ambient noise data (July 2021 to June 2022) from 24 broadband seismic stations within the Egyptian National Seismological Network and the GeoForschungsZentrum (GFZ) network. The geographical distribution of these stations covers a range of station spacing from 20 to 1000 km. The compiled dataset undergoes testing using the power spectral density (PSD) technique, as introduced by Peterson (1993). PSD serves as a valuable tool for assessing instrumental anomalies, geographical disparities, proximity to local noise sources, and diurnal and seasonal fluctuations.

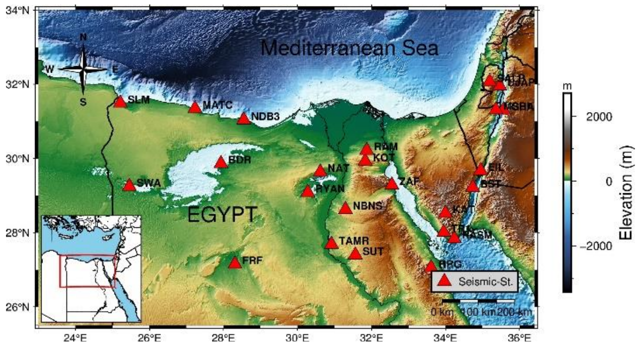

Figure 1. A tomographic map of the study area. Red triangles refer to the distribution of 24 broadband seismic stations used in this study.

3. METHODOLOGY AND RESULTS

Bensen et al. (2007) introduced a comprehensive framework for processing ambient noise data with a primary focus on its application in surface wave tomography, specifically for Rayleigh waves. The proposed approach comprised four distinct phases: (Phase 1) preprocessing of data obtained from individual stations; (Phase 2) cross-correlation (CC) and stacking procedures essential for enhancing the signal-to-noise ratio; (Phase 3) extraction of the observed dispersion curves that are crucial for further analysis; and (Phase 4) tomographic inversion for subsurface imaging.

3.1. Phase 1: Single Station Data Preparation

After collecting of the vertical-component ambient noise data from 24 stations and testing the quality, we selected the data based on the daily waveform of more than 80%. The data gap between traces must be less than 25 s and filled with zero amplitude. First, the instrument response was removed to eliminate any instrumental artifact. Next, the data underwent demeaning, detrending, and tapering operations to remove any mean offsets, long-term trends, and potential spurious signals that may interfere with the analysis. Subsequently, the data were filtered on a 5 to 50 s period range and downsampled from the initial 100 SPS to 1 SPS. Temporal normalization techniques were employed in the time domain to mitigate the influence of the local earthquake signals and local seismicity on the data. Then spectral whitening is applied in the frequency domain to remove the secondary microseismic band from the data.

3.2. Phase 2: Cross-Correlation and Time Stacking

ANT utilizes CC to multiply the signals of two stations and integrate them over a time series period, deriving a time delay, called Green's Function. The cross-correlation function (CCF) is computed daily using the raw data for each station pair. These daily, monthly, and yearly results are stacked to yield a longer time series, which enhances the SNR. The recorded signals from both receivers were then subjected to a CC analysis that provides the CCF (CAB(τ)) of ambient noise uA(t) and uB(t) at stations A and B, respectively.

$$C_{AB}(\tau) = \int u_A(t)\boldsymbol{u}_B(t+\tau)dt \qquad (1)$$

where, τ represents the time shift or delay time. The [N (N − 1) / 2] formula was utilized to determine the total number of possible station pairs, where N represents the number of seismic stations used. Our dataset resulted in approximately 276 station pairs, from which we obtained the CCFs. The CCF results were stored as two-sided time functions encompassing positive and negative time lags. The time lags represent the time delay between the signals proportional to the separation distance between the two stations and the Rayleigh wave velocity of the medium. The results of CC are recorded in positive and negative time lag shown in Figure 2, which represents the waves traveling between the station pairs in opposite directions (Bensen et al., 2007). The GF was computed as the time derivative of the average of the positive time lag signal $(C\_AB(t))$ and its corresponding negative time lag signal $(C\_(AB)(-t))$ $(Eq.(2))$:

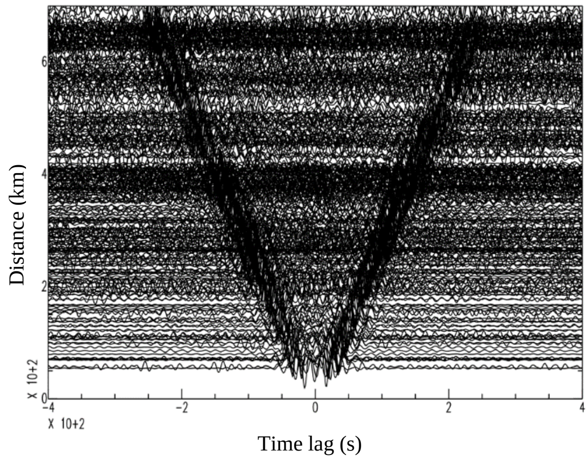

Figure 2. Record section derived from 12 month of ambient noise cross-correlations (CCFs) for XX station pairs (vertical component). The CCFs were filtered between 5–50 s and normalized by absolute mean normalization and plotted as a function of interstation distance.

$$G_{AB}(t) = -\frac{d}{dt}\left[\frac{C_{AB}(t) + C_{AB}(-t)}{2}\right] \qquad (2)$$

Note that C_AB(t) and C_(AB)(-t) represent signals with positive and negative time lags, respectively.

Obtained Signal to Noise Ratio (SNR)

SNR is defined as the ratio of the maximum amplitude of the signal window to the root mean square of the noise window. SNR is a crucial parameter indicating the CCF's quality and assisting in selecting reliable period bands for dispersion measurements. In this work, the SNR was calculated by first defining the signal window size using the minimum and maximum group arrival times (3.5/distance < t < 2.5/distance) and setting the noise window size to 500 s, starting after the trailing noise ends, that is, the end of the signal window (Bensen et al., 2007). Several factors influence the SNR value, including the following:

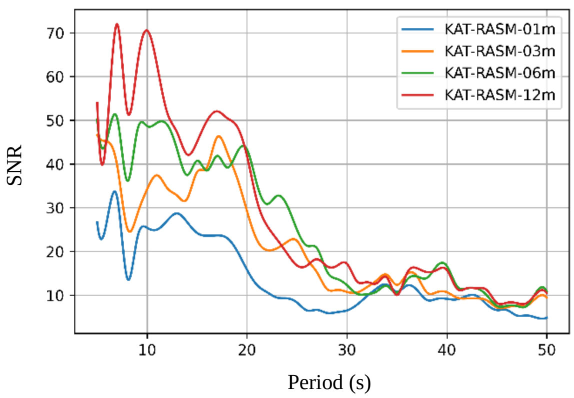

Figure 3. Four examples of spectral SNR for a CCF between two stations pairs (KAT-RASM) with station spacing 80 km, at different stacking lengths (1, 3, 6 and 12 months).

1- Time series length: The SNR generally increases with longer time series lengths (Yang et al., 2008). Hence, the more extended time series of the CCF yields improved SNR values (Figure 3).
2- Local noise conditions: The prevailing noise environment affects the SNR.
3- Interstation distance (path length): The closer station pairs show higher SNR values, especially in short periods.

3.3. Phase 3. Obtained Surface Wave Dispersion Curve

The dispersion curve was constructed by applying frequency-time analysis (FTAN) and extracting the group velocities at different frequencies (see an example in Figure 4). It depicts the relationship between the group velocity and the period for the surface waves propagating through the region of interest, as described in previous studies (Levshin & Ritzwoller, 2001; Bensen et al., 2007). Analysis of the 276 dispersion curves obtained from the 24 seismic stations revealed distinct group velocity variations across the interested area. We observed that the station pairs in the western part showed notably lower group velocities at shorter periods. In contrast, the station pairs located in the eastern part of the study area showed higher group velocities at shorter periods, with a less pronounced increase achieved as the periods lengthened.

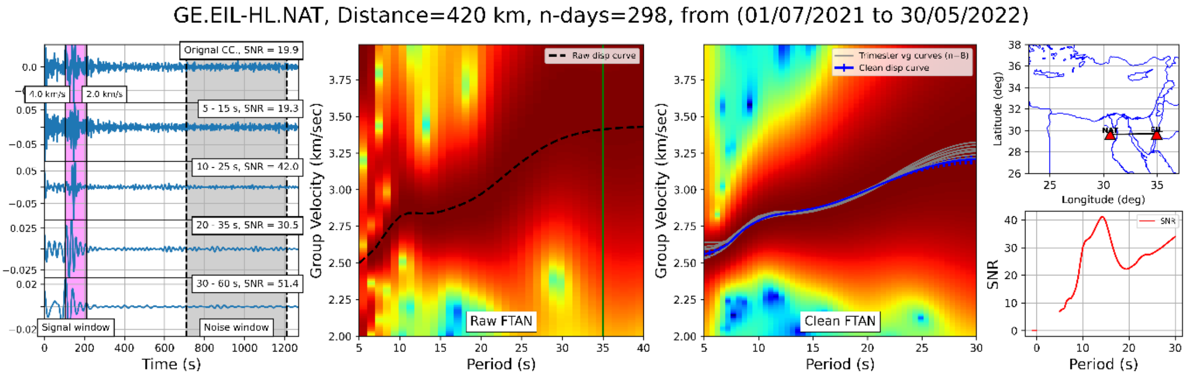

Figure 4. Examples of frequency-time analysis (FTAN) calculated from 12 months of stacked CCF for one station pair, (GE.EIL-HL.NAT). Left panel: symmetric component of the original CCF and set of Gaussian band-pass filter, signal window marked by cyan color and noise window marked by gray color, SNR and period bands are centered at each panel. Two middle panels: raw and clean FTAN and corresponding observed dispersion curves. The green vertical line represents the cut-off period, and error bars on the blue line indicate the standard deviation. Right panel: location of station pairs on the map of the study area at the top and average SNR at different periods at the bottom.

3.4. Phase 4: Tomographic Inversion Map

A tomographic inversion is a group velocity map generated by inverting the observed dispersion curves at selected periods. The inversion process is typically executed through a forward modeling algorithm that simulates the seismic wave propagation within a given subsurface model. The theoretical dispersion curves are compared with the observed data, and the discrepancies between the two are utilized to update the model parameters. This iterative process continues until the differences between the observed and synthetic data are minimized, culminating in the final and refined model of the subsurface. As outlined by Barmin et al. (2001), the tomographic method's algorithm relies on a relationship at any period T described:

$$d = GM + \sigma \quad (3)$$

where the data vector (d) represents the differences observed in the reference travel time (travel time perturbations) between the station pairs deduced from the measured group velocities at period T. The data model (M) comprises the best-fitting parameters $(v0 - v)/v$ at the grid nodes, representing slowness perturbations along the regular grid nodes. ν denotes the observed velocity derived from the dispersion curve, while $v0$ represents the reference velocity (inverse of the mean slowness). The slowness implied by the observed travel times is calculated as the sum of the observed travel times divided by the sum of the interstation distances. The forward matrix (G) is a coefficient that facilitates slowness integration along the wave paths. σ denotes the standard deviation for d.

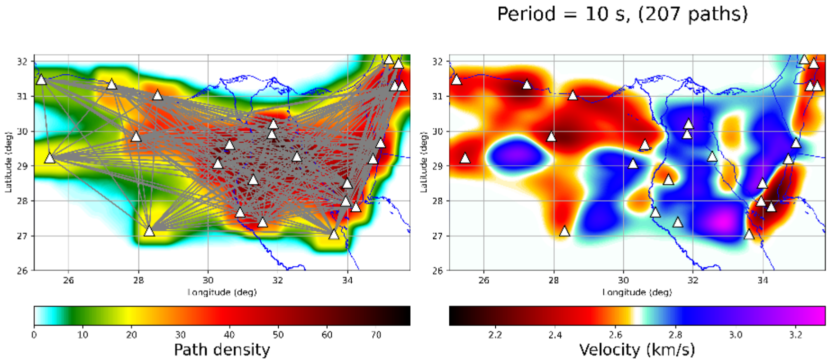

Figure 5. Examples of Rayleigh wave group velocity map at periods 10 s. Left panel: path densities for each grid node. Middle panel: group velocity distribution. White-colored areas are those without ray path coverage. Right-panel: spatial resolution map from 50 to 500 km. White triangles refer to the seismic stations used in this study.

4- ONE DIMENSIONAL SHEAR WAVE VELOCITY MODEL

After obtaining the observed dispersion curve at any selected point from the group velocity map, we inverted the information to shear wave velocity with depth. The inverse problem of determining the input data from the given output data was addressed by using the Markov Chain Monte Carlo (MCMC) method employing the Metropolis algorithm (Mosegaard & Tarantola, 1995). The misfit value of the calculated dispersion curve to the observed dispersion curve is derived as follows:

$$S(m) = \sum_{i=1}^{N} \frac{(v_g^m(T_i) - v_g^{obs}(T_i))^2}{2\sigma^2(T_i)} \tag{4}$$

where, v_g^m and v_g^{obs} σ represent the calculated and observed dispersion curves, respectively, and σ denotes the standard deviation of the observed dispersion curve at period Ti. When we compare the results of the Moho depth from this study by using ANT and previous work from the joint inversion of receiver function and surface wave dispersion method (Hosny & Nyblade, 2016), we can see no big differences at the same points, for example at FRF and KOT stations located at Eastern Desert and Western Desert respectively, the Moho discontinuity located at 41.4 ± 2.37 km at FRF and 36 ± 2.0 km at KOT stations, that coincide with the previous results, while the Moho discontinuity is located at 35 and 38 km at FRF and KOT respectively.

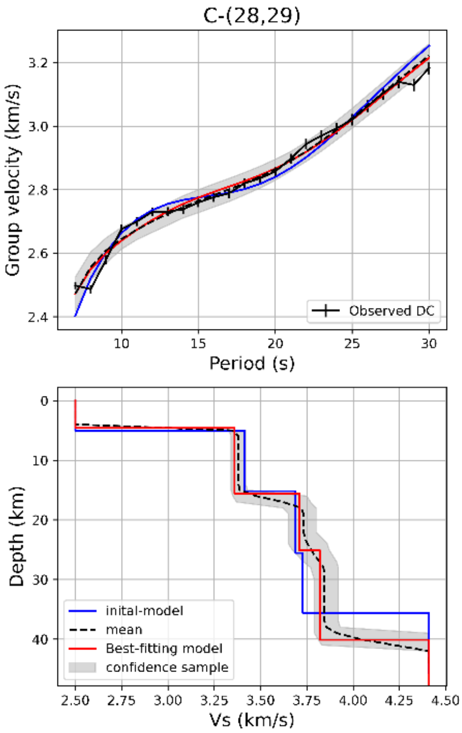

Figure 6. Ensemble models of one-dimensional inversion of group velocity dispersion curve at point C in the Northwestern Desert. The black line in the upper figure indicates the observed dispersion curve, error bars are the stander deviations around the group velocities. The gray color is represented 95 % of the 5000-confidence sampled interval of theoretical group velocities function of the period (upper) and corresponding shear velocity function of depth (lower). Theoretical group velocities function of the period (upper) inverted to initial models (lower). Black

dotted lines mean confidence sampled dispersion curves (upper), and the mean of corresponding models (lower). Red lines in the upper and middle figures are the best-fitting models.

5. CONCLUSIONS

This study aimed to investigate the crustal structure of the upper and lower crust in Northern Egypt Continuous seismic data collected over a 12-month period from 24 vertical component broadband permanent seismic stations within the region were used in this work. The ANT data processing comprised four essential steps: 1- preprocessing, 2- Cross-correlation analysis for 276 station pairs to derive Green's Functions and stacking the results for one year, 3- Obtaining Rayleigh-wave group velocity dispersion curve by applying FTAN to the time lag of the CC results for each station pair. 4- Construction of group velocity map for periods ranging from 5 to 30 s. Our study area can be delineated into distinct zones characterized by varying velocities based on the group velocity map analysis. The eastern region encompassing the Sinai Peninsula and Northeastern Desert exhibits high-velocity values, while the Northwestern Desert constitutes a low-velocity zone. The Nile River acts as a natural boundary demarcating these two primary regions. Velocity anomalies were also observed, with certain areas in the eastern high-velocity zone displaying lower velocities, and vice versa, in the western low-velocity zone. The Metropolis algorithm method was employed to develop one-dimensional shear wave velocity models at each grid point. The estimated Moho depths are between 40 km in the Southwestern Desert to 35 km in the Northeastern Desert and Sinai Peninsula. This approach enables the exploration of possible velocity models and the identification of the best-fitting model for the subsurface structure.

ACKNOWLEDGEMENTS

I would like to express my heartfelt gratitude and appreciation to everyone who has contributed to my academic journey and enriched my experience during this course. First and foremost, I extend my deepest thanks to my supervisor, Dr. Takumi Hayashida, for his unwavering support and guidance throughout this course and my master's work. I would also like to acknowledge Dr. Tatsuhiko Hara, the course leader, for his valuable support, insightful comments, and helpful advice during our individual study. Additionally, I extend my thanks to all the esteemed staff members at IISEE/BRI whose expertise and teachings have contributed significantly to my learning experience. It fills me with pride to have learned from such knowledgeable individuals.

REFERENCES

Collins, A. S., Blades, M. L., & Merdith, A. S. (2021). The Arabian–Nubian Shield Within the Neoproterozoic Plate Tectonic Circuit. The Geology of the Arabian-Nubian Shield, 195-202.

Peterson, J. (1993). Observations and modeling of background seismic noise. US Geol. Surv. Open-File Rept, 9(3).

Bensen, G., Ritzwoller, M., Barmin, M., Levshin, A. L., Lin, F., Moschetti, M., . . . Yang, Y. (2007). Processing seismic ambient noise data to obtain reliable broad-band surface wave dispersion measurements. Geophysical journal international, 169(3), 1239-1260.

Barmin, M. P., Ritzwoller, M. H., & Levshin, A. L. (2001). A fast and reliable method for surface wave tomography. Monitoring the comprehensive nuclear-test-ban treaty: Surface waves, 1351-1375.

Levshin, A., & Ritzwoller, M. (2001). Automated detection, extraction, and measurement of regional surface waves. Monitoring the comprehensive nuclear-test-ban treaty: Surface waves, 1531-1545.

Goutorbe, B., de Oliveira Coelho, D. L., & Drouet, S. (2015). Rayleigh wave group velocities at periods of 6–23 s across Brazil from ambient noise tomography. Geophysical Journal International, 203(2), 869-882.

Hosny, A., & Nyblade, A. (2016). The crustal structure of Egypt and the northern Red Sea region. Tectonophysics, 687, 257-267.

Mosegaard, K., & Tarantola, A. (1995). Monte Carlo sampling of solutions to inverse problems. Journal of Geophysical Research: Solid Earth, 100(B7), 12431-12447.